energies

MDPI

Article

Modeling and Performance Assessment of the Split-Pi Used as a Storage Converter in All the Possible DC Microgrid Scenarios. Part II: Simulation and Experimental Results

Massimiliano Luna [1], Antonino Sferlazza [2], Angelo Accetta [1], Maria Carmela Di Piazza [1,*], Giuseppe La Tona [1] and Marcello Pucci [1]

[1] Istituto di Ingegneria del Mare (INM), Consiglio Nazionale delle Ricerche (CNR), Via Ugo La Malfa 153, 90146 Palermo, Italy; massimiliano.luna@cnr.it (M.L.); angelo.accetta@cnr.it (A.A.); giuseppe.latona@cnr.it (G.L.T.); marcello.pucci@cnr.it (M.P.)

[2] Dipartimento di Ingegneria (DI), Università degli Studi di Palermo, Viale delle Scienze Ed. 10, 90128 Palermo, Italy; antonino.sferlazza@unipa.it

* Correspondence: mariacarmela.dipiazza@cnr.it

Abstract: Bidirectional DC/DC converters such as the Split-pi can be used to integrate an energy storage system (ESS) into a DC microgrid providing manifold benefits. However, this integration deserves careful design because the ESS converter must behave like a stiff voltage generator, a non-stiff voltage generator, or a current generator depending on the microgrid configuration. Part I of this work presented a comprehensive theoretical analysis of the Split-pi used as an ESS converter in all the possible DC microgrid scenarios. Five typical microgrid scenarios were identified. Each of them required a specific state-space model of the Split-pi and a suitable control scheme. The present paper completes the study validating the theoretical analysis based on simulations and experimental tests. The chosen case study encompassed a 48 V, 750 W storage system interfaced with a 180 V DC microgrid using a Split-pi converter. It can represent a reduced-power prototype of terrestrial and marine microgrids. A prototypal Split-pi converter was realized in the lab, and several experimental tests were performed to assess the performance in each scenario. The results obtained from the experimental tests were coherent with the simulations and validated the study.

Keywords: Split-pi; bidirectional converter; electrical storage system; DC microgrid; droop control; current control; feed-forward control

Citation: Luna, M.; Sferlazza, A.; Accetta, A.; Di Piazza, M.C.; La Tona, G.; Pucci, M. Modeling and Performance Assessment of the Split-Pi Used as a Storage Converter in All the Possible DC Microgrid Scenarios. Part II: Simulation and Experimental Results. *Energies* **2021**, *14*, 5616. https://doi.org/10.3390/en14185616

Academic Editor: Mohamed Benbouzid

Received: 12 July 2021
Accepted: 3 September 2021
Published: 7 September 2021

1. Introduction

Low voltage DC microgrids present well-known advantages over AC microgrids, such as increased efficiency, lower cost, simplified power electronic converters and related control systems, as well as easier power flow management. In general, their voltage level depends on the rated power. In fact, for a given power level, a higher voltage allows reducing the circulating currents and, in turn, the cross-section of the conductors; thus, a reduction of volume, weight, and cost can be attained by increasing the voltage level.

DC microgrids in stationary applications are mainly proposed for residential and commercial buildings with load powers ranging from 1 kW to hundreds of kilowatts. As explained in [1–3], several possibilities exist for their rated voltage. Typically, the rated DC voltage is chosen coherently with the standard AC ratings, i.e., 120 V DC, 230 V DC, or 400 V DC. Alternatively, if the DC microgrid is supplied by a passive diode rectifier connected to the mains, its voltage equals the rectified mains (i.e., 170 V DC, 325 V DC, or 566 V DC). Finally, if an active rectifier supplies the DC microgrid and the latter encompasses AC loads supplied by an inverter, slightly higher values than the rectified mains must be chosen to provide a suitable margin for voltage regulation.

As for DC microgrids in mobile applications, whenever possible, 48 V DC is chosen to exploit the advantages of Safety Extra-Low Voltage (SELV) systems. However, the rated

power of the electrical equipment used in mobile applications is constantly increasing, and so does the nominal DC voltage. Contrarily to the 270 V DC bus imposed to aircraft and unmanned aerial vehicles (UAVs) by the standard MIL-STD-704F [4], no specific voltage level has been established for marine applications, except for large vessels and cruise ships, where 1 kV or 1.5 kV DC is commonly chosen.

For example, a 120 V DC microgrid supplied the 5 kW load of the small underwater remotely operated vehicle (ROV) described in [5]. Additionally, 200 V DC microgrids were considered as case studies in [6] and [7]. In the first case, a 1 kW docking system with bidirectional wireless power transmission capability was proposed for an autonomous underwater vehicle (AUV). In the other case, a centralized stabilizer was designed for a marine DC microgrid used in offshore and ship applications. A 400 V marine DC microgrid was considered in [8] and [9]. In particular, the microgrid of [8] was supplied by a fuel cell and delivered up to 90 kW to the electrical loads of a sailing boat; instead, the shipboard microgrid of [9] encompassed a 400 kW storage system, and it was studied to devise a power management strategy. A 500 V DC shipboard microgrid with two buses and two synchronous generators with 35 kW of total installed power was considered in [10]. Finally, shipboard microgrids with rated voltage ranging from 700 to 750 V DC were considered as case studies in [11] and [12]. In the first case, the microgrid supplied a 12 kW load connected to a 700 V DC bus, and a distributed secondary control strategy was proposed. In the other case, the microgrid of a ferry vessel was modeled for fuel cell integration studies; three 800 kW fuel cells powered three interconnected DC busbars at 750 V DC.

In any case, DC distribution in terrestrial and marine power systems requires extensive use of power electronic converters to interface distributed generation units, loads, and electrical storage systems (ESSs) [13–15]. In particular, bidirectional DC/DC converters are exploited to integrate ESSs into DC microgrids providing manifold benefits such as improved stability and resiliency, compensation of renewable generator's fluctuations, ramping support to generators, and the possibility to employ suitable energy management systems (EMSs) to optimize microgrid power flows [13,16–18].

Among the several topologies of bidirectional DC-DC power converters, the Split-pi is receiving increasing attention due to its distinct advantages such as high efficiency, reduced switch count, small reactive components and switching noise, as well as suitability for multiphase systems, at the only cost of non-isolated operation [19–27]. However, none of the previous works on the Split-pi focused on the connection to DC microgrids. Furthermore, only three papers proposed applications in which such a converter was not controlled in an open-loop fashion [23,24,26]. Such papers, however, presented only closed-loop applications with a single control loop; furthermore, they neglected the reactive components' parasitic resistances and did not perform any experimental validation.

On the other hand, the integration of DC-DC bidirectional converters into a DC microgrid requires a careful design of the power converter's control system, depending on how the microgrid voltage is controlled (stiff voltage control by a single generator, multiple droop-controlled voltage generators respecting a predefined power-sharing ratio or master-slave control supervised by an EMS). To the best of the authors' knowledge, no paper in the technical literature presented a comprehensive analysis of all the scenarios in which a bidirectional DC/DC converter can be used to interface an ESS with a DC microgrid. The traced contributions fall into two categories. On the one hand, many authors presented a specific converter topology for microgrid applications but modeled the converter considering its output closed on either a load resistor or an ideal voltage source. Therefore, the respect of the chosen stability margin was not guaranteed in real applications where mixed loads stem from the combination of passive loads, droop-controlled voltage generators, and current sources controlled by EMSs. On the other hand, other authors modeled the whole microgrid based on power system or control approaches with different goals such as assessing stabilization and fault or power management techniques or minimizing circulating currents. Thus, such studies were focused on a higher operation level than the present work.

This paper is the second part of a work aimed at analyzing all the scenarios in which a bidirectional DC/DC converter is used to interface an ESS with a DC microgrid. Part I dealt with the theoretical aspects of the problem [28]. First, the five possible DC microgrid scenarios were identified. Then, it was shown that a specific state-space model and a suitable control scheme were required to obtain high performance from the Split-pi in each scenario. The proposed models (denoted as models A and B) considered the parasitic resistances. The control schemes required two to three control loops plus a feed-forward (FF) action depending on the scenario. Finally, a more complex compensator than a conventional PI regulator was needed for output current control in stiff microgrids.

The present paper completes the study proposed in part I, validating the theoretical analysis based on a comprehensive set of simulations and experimental tests. Due to constraints imposed by the available lab equipment, a 180 V DC, 750 W microgrid was chosen as a case study. It can represent a reduced-power prototype of terrestrial and marine microgrids, e.g., a residential DC microgrid encompassing 120 V AC loads supplied by an inverter or the DC microgrid onboard a small-power ROV or AUV. Such an approach is coherent with [29], in which the microgrid of an electric ferry powered by fuel cells was scaled down to 110 V DC, 500 W to validate a stability enhancement technique. In any case, the choice of the voltage rating of the microgrid does not affect the validity of the conclusions, which can be straightforwardly extended to the whole range of low voltage DC.

A prototype of the Split-pi converter was realized in the lab to interface an emulated 48 V ESS with the 180 V microgrid. Then, several experimental tests were performed to assess the performance in each scenario. The results obtained from the experimental tests were coherent with the simulations and validated the study. Finally, it is worth remarking on the general validity of the proposed approach, which can also be followed when other bidirectional DC/DC converter topologies are employed to interface an ESS with a DC microgrid.

2. Overview of the DC Microgrid Scenarios for the Operation of the Split-pi as an ESS Converter

The complete theoretical analysis of the DC microgrid scenarios, state-space models, and required control schemes for the Split-pi converter used as an ESS converter (i.e., operating with lower storage-side voltage than grid-side voltage) was presented in Part I of the present work. In the following, only the main concepts will be recalled to ease the interpretation of the simulations and the experimental results.

Five scenarios can be considered depending on the control mode chosen for the storage-side converter (interfacing the ESS) and the grid-side converters (interfacing other microgrid generators, if any). They are described in Table 1, which summarizes the corresponding table reported in Part I of the present work. In particular, the first three columns describe each scenario; the fourth and fifth columns, instead, associate to each scenario the state-space model and the control scheme required for the Split-pi, which were devised in Part I.

For the sake of clarity, the five scenarios are referred to also using an abbreviation in the form Sx-Gy, where x and y specify the control mode for the storage-side and the grid-side converters, respectively. The range of options for x is:

- C for current control.
- D for non-stiff droop control.
- S for stiff droop control.

Table 1. Possible combinations of microgrid scenarios, converter models, and control schemes for the Split-pi.

Microgrid Scenario	Storage Converter	Other Generators	State-Space Model of the Split-pi	Control Scheme
#1 (SS-GN)	Droop mode with $R_d = 0$ (stiff microgrid)	No other generator present (passive load) or all current controlled by the EMS	Model A	2 loops (I_{L1} and V_2) + FF
#2 (SD-GN)	Droop mode with $R_d \neq 0$	No other generator present (passive load) or all current controlled by the EMS	Model A	3 loops (I_{L1}, V_2, and droop) + FF
#3 (SD-GD)	Droop mode with $R_d \neq 0$	At least one is droop controlled and none has $R_d = 0$	Model A	3 loops (I_{L1}, V_2, and droop) + FF
#4 (SC-GD)	Current mode	At least one is droop controlled and none has $R_d = 0$	Model A	2 loops (I_{L1} and I_{L2})
#5 (SC-GS)	Current mode	One is droop controlled and has $R_d = 0$ (stiff microgrid); the others, if present, are current controlled by the EMS	Model B	2 loops (I_{L1} and I_{L2})

Furthermore, a baseline scenario derived from scenario #1 excluding the FF action was also considered for comparison purposes to show the usefulness of such action.

3. Overview of the Chosen Case Study and Droop Characteristics of the Storage-Side and Grid-Side Converters

The considered case study encompassed a 48 V, 750 W storage system interfaced with a 180 V DC microgrid using a Split-pi converter. As explained in the Introduction, it can represent a reduced-power prototype of terrestrial and marine microgrids. Figure 1 shows the schematic of the Split-pi converter, which was sized for the chosen case study in Part I of the present work. Its main parameters are summarized in Table 2. Furthermore, in Part I of the work, five control systems were designed, i.e., one for each specific scenario. It was assumed that the converter supplied its rated power without an external current or voltage generator. The latter was seen as a disturbance, which the control system had to compensate promptly. Furthermore, suitably wide stability margins were imposed, so the designed controllers were also effective at lighter loads.

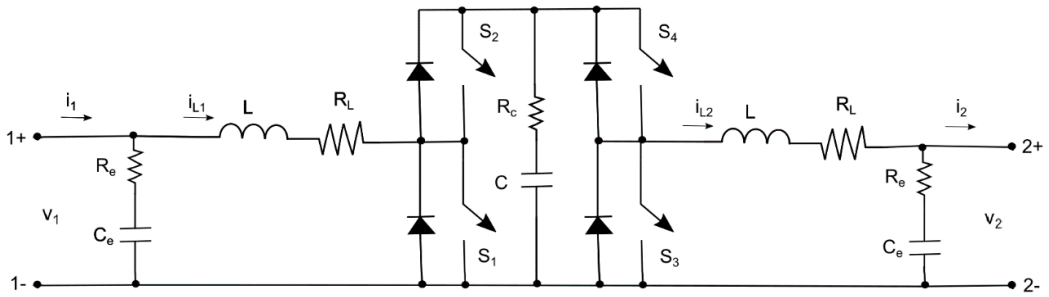

Figure 1. Schematic of the Split−pi converter.

For a proper interpretation of the simulation results, it is worth recalling the droop characteristics of both the storage converter and the voltage generator of the microgrid. As for the storage converter, its droop characteristic was defined by $E_{ds} = 180$ V and $R_{ds} = 0$ in scenario #1 (SS-GN); in scenarios #2 (SD-GN) and #3 (SD-GD), instead, it was expressed by $E_{ds} = 180$ V and $R_{ds} = 2.2\ \Omega$, i.e., imposing a 5% voltage reduction at the nominal current. As for the equivalent voltage generator of the microgrid, its droop parameters were equal to those of the storage converter in scenario #4 (SC-GD). Instead, in scenario #3 (SD-GD), they were expressed by $E_d = 198$ V and $R_d = 9\ \Omega$; thus, the storage system did not supply any power for half the rated load of the microgrid, as desired. Finally, in scenario #5 (SC-GS), a constant voltage generator $E_d = 180$ V was considered to model the microgrid's stiff voltage generator.

Table 2. Main parameters of the Split-pi converter.

Parameter	Symbol	Value
Switching frequency	F_{sw}	20 kHz
Nominal output voltage	V_{2n}	180 V
Nominal input voltage	V_{1n}	50 V
Nominal power	P_n	750 W
Nominal load resistance	R_n	43.2 Ω
Nominal input current	I_{1n}	15 A
Max. charge/discharge current	I_{cx}, I_{dx}	18 A
Nominal output current	I_{2n}	4.167 A
Nominal duty-cycle	$\overline{d}$	0.722
Inductance value of L	L	1000 µH
Parasitic resistance of L	R_L	65 mΩ
Capacitance value of C_e	C_e	200 µF
Parasitic resistance of C_e	R_e	260 mΩ
Capacitance value of C	C	540 µF
Parasitic resistance of C	R_c	125 mΩ
Max. ripple on input/output inductors	$r_{i\%}$	±6.0%
Max. ripple on input/output capacitors	$r_{ve\%}$	±0.2%
Max. ripple on bulk capacitor	$r_{v\%}$	±0.2%

4. Simulation Results

Several simulations were performed to assess the performance of the controlled system in all the scenarios. The circuit model was implemented using PLECS based on the electrical parameters of Table 2, whereas the control system was realized in Simulink. The simulation parameters set in the Simulink environment were the following:

- solver type: variable-step
- solver: ode23tb (stiff/TR-BDF2)
- max step size: $1/(10 \cdot F_{sw})$
- solver reset method: robust.

The default values were confirmed for the other Simulink parameters, as well as for the PLECS parameters. The obtained simulation results are presented and commented on in the following.

4.1. Validation of FF Action and Performance Assessment in Scenario #1 (SS-GN)

As a starting point to prove the advantage of the FF action, the baseline scenario in which the storage converter supplied a microgrid stiffly at 180 V was simulated. Besides the passive load, a current generator was also present in the microgrid. Only the two innermost control loops for I_{L1} and V_2 were employed, the FF action was disabled, and the system was described by state-space model A.

The waveforms of the most meaningful electrical and control quantities are shown in Figures 2 and 3a. Before t = 0.2 s, the converter output was at a steady state with the following values of load resistance, load power, and external current reference: $R = R_n$, $P = P_n$, and $I = 0$. Then, a representative sequence of R and I values was applied, as shown in Table 3. From t = 0.2 s to t = 0.6 s, the load was passive and exhibited two stepwise variations from the rated power almost to a no-load condition and vice versa. At t = 0.6 s, the load resistance was kept constant, but the external current reference was increased to supply the load fully; hence, the converter's output current dropped to zero. Then, at t = 0.8 s, the converter operated again with a very low load, so the external current was almost entirely fed back to the converter to recharge the storage system at full power. At t = 1 s, the load power was increased to its rated value. Finally, the sequence applied during the remaining time intervals was such that the external current generator started and stopped recharging the storage system at full power while the load resistance was the rated one.

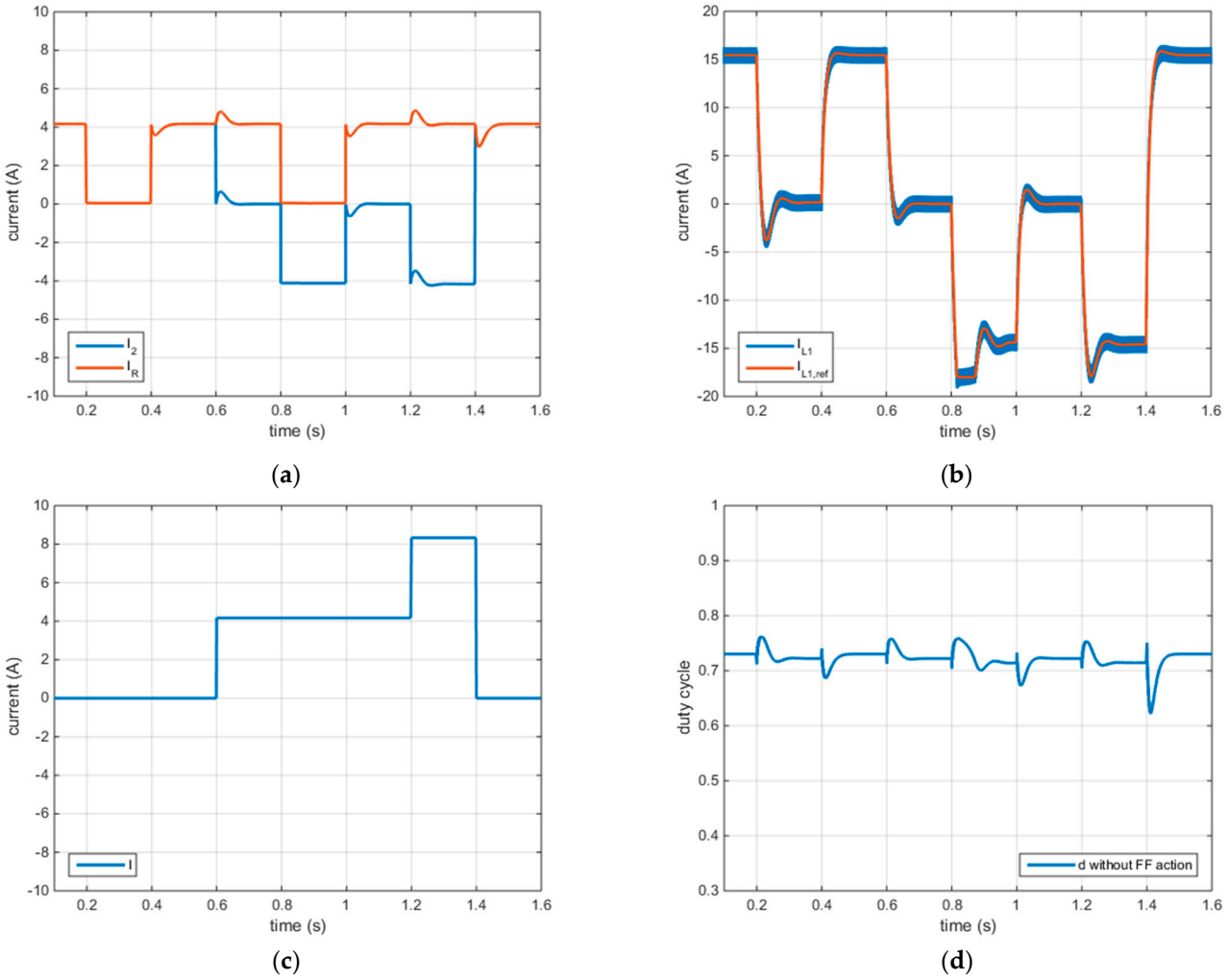

Figure 2. Baseline performance without FF action: (**a**) output current and load current; (**b**) input inductor current; (**c**) external generator's current; (**d**) duty cycle.

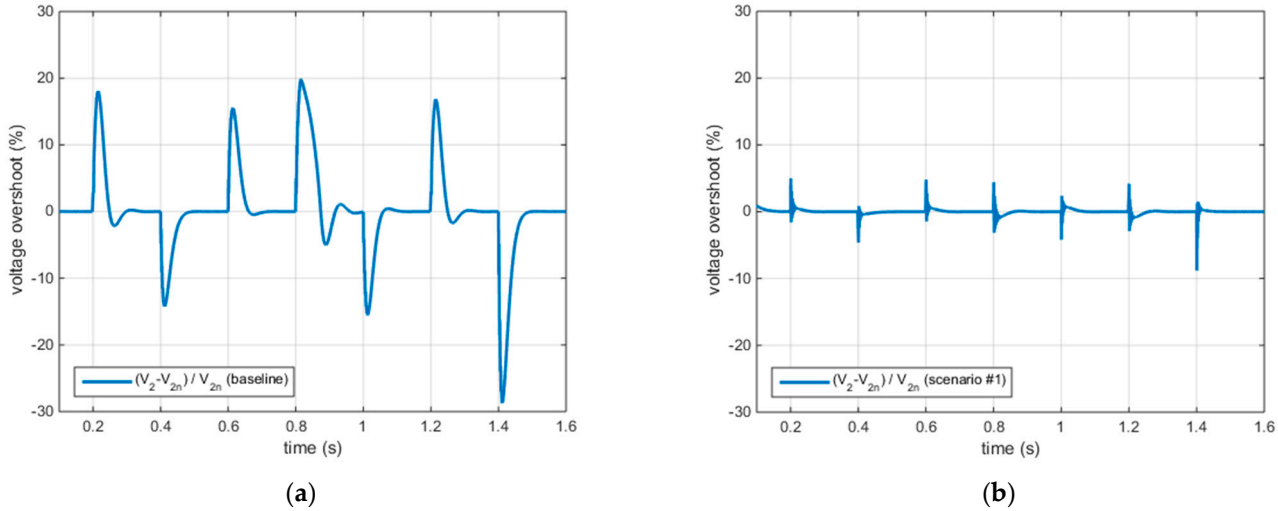

Figure 3. Grid voltage overshoot: (**a**) in baseline scenario; (**b**) in scenario #1 (SS−GN).

Table 3. Transitions considered in the baseline scenario and scenarios #1 (SS-GN) and #2 (SD-GN).

Time (s)	Load Resistance	Expected Load Power	External Current Reference
0.2	$100 \cdot R_n$	$P_n/100$	0
0.4	R_n	P_n	0
0.6	R_n	P_n	I_{2n}
0.8	$100 \cdot R_n$	$P_n/100$	I_{2n}
1.0	R_n	P_n	I_{2n}
1.2	R_n	P_n	$2 \cdot I_{2n}$
1.4	R_n	P_n	0

The normalized waveform of grid voltage is presented in Figure 3a and shows that the converter's output voltage was correctly regulated at the desired steady-state value as the passive/active load varied. As shown in Figure 2, the current loop dynamics were fast enough to track $I_{L1,ref}$ instantly. However, the voltage waveform exhibited significant under- and overshoots due to load variations, as shown in Figure 3a. In particular, the maximum overshoot and undershoot were 20% and −29%, respectively. On the other hand, the microgrid usually has an allowed transient voltage tolerance of ±20% around its nominal voltage, so it would have been automatically de-energized by the protection devices, causing severe inconvenience.

A significant improvement of the system response can be achieved using the FF action; therefore, such action was enabled in the first three scenarios of Table 1, starting from scenario #1 (SS-GN). The difference between such a scenario and the baseline one is only the inclusion of the FF action. The related simulation results are shown in Figures 3b and 4. As shown in Figure 4d, the FF action varied the duty cycle instantaneously to compensate for the load variation. Consequently, the waveforms of I_{L1}, I_2, and I_R were pretty squared (Figure 4a,b), and the resulting output voltage exhibited acceptable over/undershoots (5% and −8.8%), as shown in Figure 3b. Thus, a correct operation of the microgrid was attained.

4.2. Performance Assessment in Scenario #2 (SD-GN)

Unlike the first scenario, in scenario #2 (SD-GN), the storage converter was controlled using a droop scheme with $R_d \neq 0$, i.e., with three control loops (I_{L1}, V_2, and droop) plus the FF action. All the other parameters, including the initial conditions and load sequence, were kept unchanged. The microgrid voltage was not constant at 180 V at steady-state due to the droop control; thus, the actual load power was slightly lower than the value reported in Table 3 depending on voltage reduction, as expected.

The simulation results in terms of grid voltage waveforms are shown in Figure 5. The converter's output voltage (V_2) quickly tracked the reference voltage (V_{2ref}) computed according to the droop characteristic during the entire timeframe. In particular, the voltage variation was ±5% when the storage system was discharged/recharged at the rated current, as expected based on the droop characteristic. The over/undershoot superimposed to the steady-state voltage variation was less than ±1.66%. Thus, the microgrid voltage stayed within ±7% of its rated value even during transients. The input/output currents and duty cycle were not shown because their waveforms were like those obtained in scenario #1 (SS-GN).

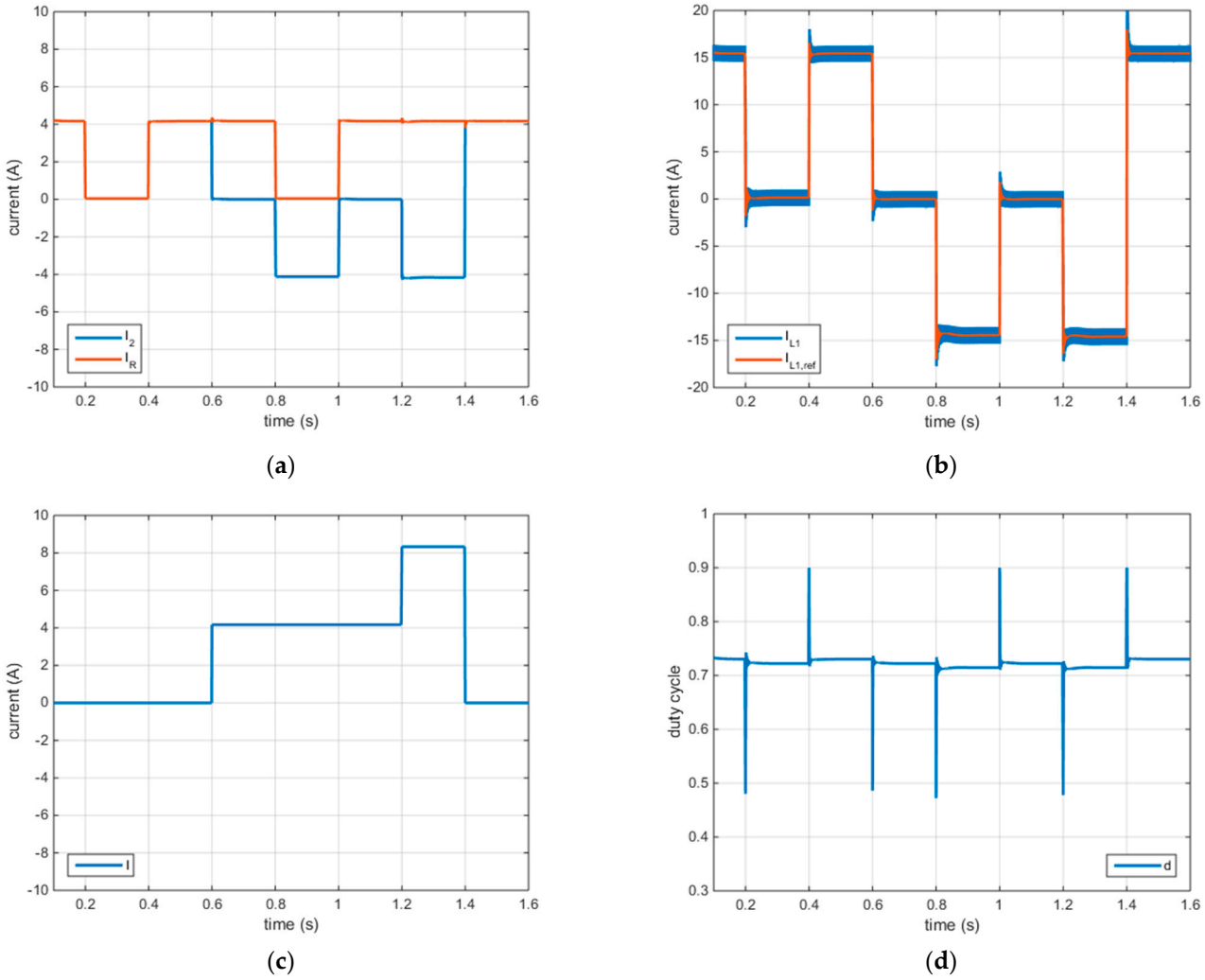

Figure 4. Performance obtained in scenario #1 (SS−GN): (**a**) output current and load current; (**b**) input inductor current; (**c**) external generator's current; (**d**) duty cycle.

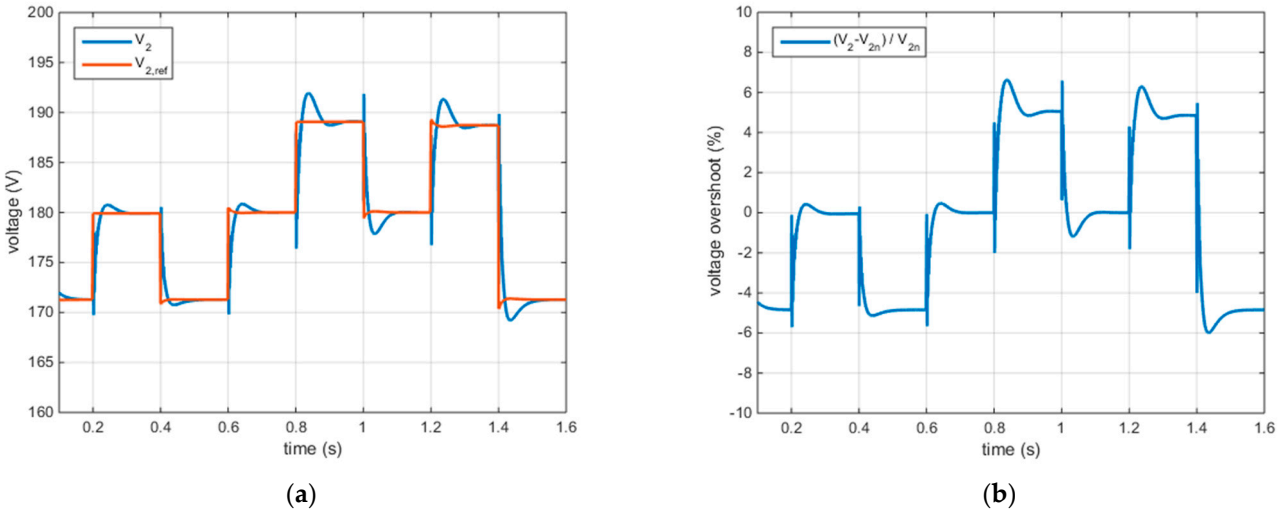

Figure 5. Performance obtained in scenario #2 (SD−GN): (**a**) actual and reference grid voltage; (**b**) grid voltage overshoot.

4.3. Performance Assessment in Scenario #3 (SD-GD)

In this scenario, both the storage converter and the equivalent voltage generator of the microgrid were controlled in droop mode with non-null droop resistances. Furthermore, the presence of an equivalent current generator in the microgrid was considered as well. The two droop characteristics were chosen so that the storage system did not supply any power for half the microgrid's rated load, as described in Section 3. Again, before t = 0.2 s, the converter output was at steady-state with the following values of load resistance, load power, and external current reference: $R = R_n$, $P = P_n$, and $I = 0$. However, the storage system delivered about half the rated power in this scenario, and the equivalent voltage generator supplied the remaining quota.

The load sequence that was applied to the converter after t = 0.2 s is shown in Table 4. It is like that of Table 3, with additional conditions in which the passive load drew half the rated power. Furthermore, the current reference values were chosen to inject the maximum allowed current that did not overload the droop-controlled generator and the storage system.

Table 4. Transitions considered in scenario #3 (SD-GD).

Time (s)	Load Resistance	Expected Load Power	External Current Reference
0.2	$2 \cdot R_n$	$P_n/2$	0
0.4	$100 \cdot R_n$	$P_n/100$	0
0.6	$100 \cdot R_n$	$P_n/100$	$0.75 \cdot I_{2n}$
0.8	$2 \cdot R_n$	$P_n/2$	$0.75 \cdot I_{2n}$
1.0	R_n	P_n	$0.75 \cdot I_{2n}$
1.2	R_n	P_n	$1.8 \cdot I_{2n}$

The simulation results for this scenario are shown in Figure 6. At t = 0.2 s, the external current reference was null while the load resistance doubled; hence, the converter's output current dropped to zero, as expected. At t = 0.4 s, the converter operated almost at no load, so the storage system was recharged at about half power. Then, at t = 0.6 s, the equivalent current generator injected current into the grid providing excess power; hence, the storage system was recharged at full power. From t = 0.8 s to t = 1.2 s, the load power increased from low to medium to high. The equivalent current generator injected constant current, so the charging power progressively decreased as the load power increased. Finally, at t = 1.2 s, the external current generator charged the storage system at the maximum power level besides supplying the rated load.

As in the previous scenario, the converter's output voltage quickly tracked the reference voltage computed according to its droop characteristic based on the output current; however, in scenario #3, the current also depended on the droop characteristic of the equivalent voltage generator. In particular, Figure 6d shows that the voltage variation of the microgrid was even lower compared to scenario #2 (SD-GN): from −2% to 5% at steady-state with minimal over/undershoots (i.e., less than ±1.05%). Finally, the waveforms of the input inductor current I_{L1} and the duty cycle d were not shown because they were like those obtained in scenario #1 (SS-GN).

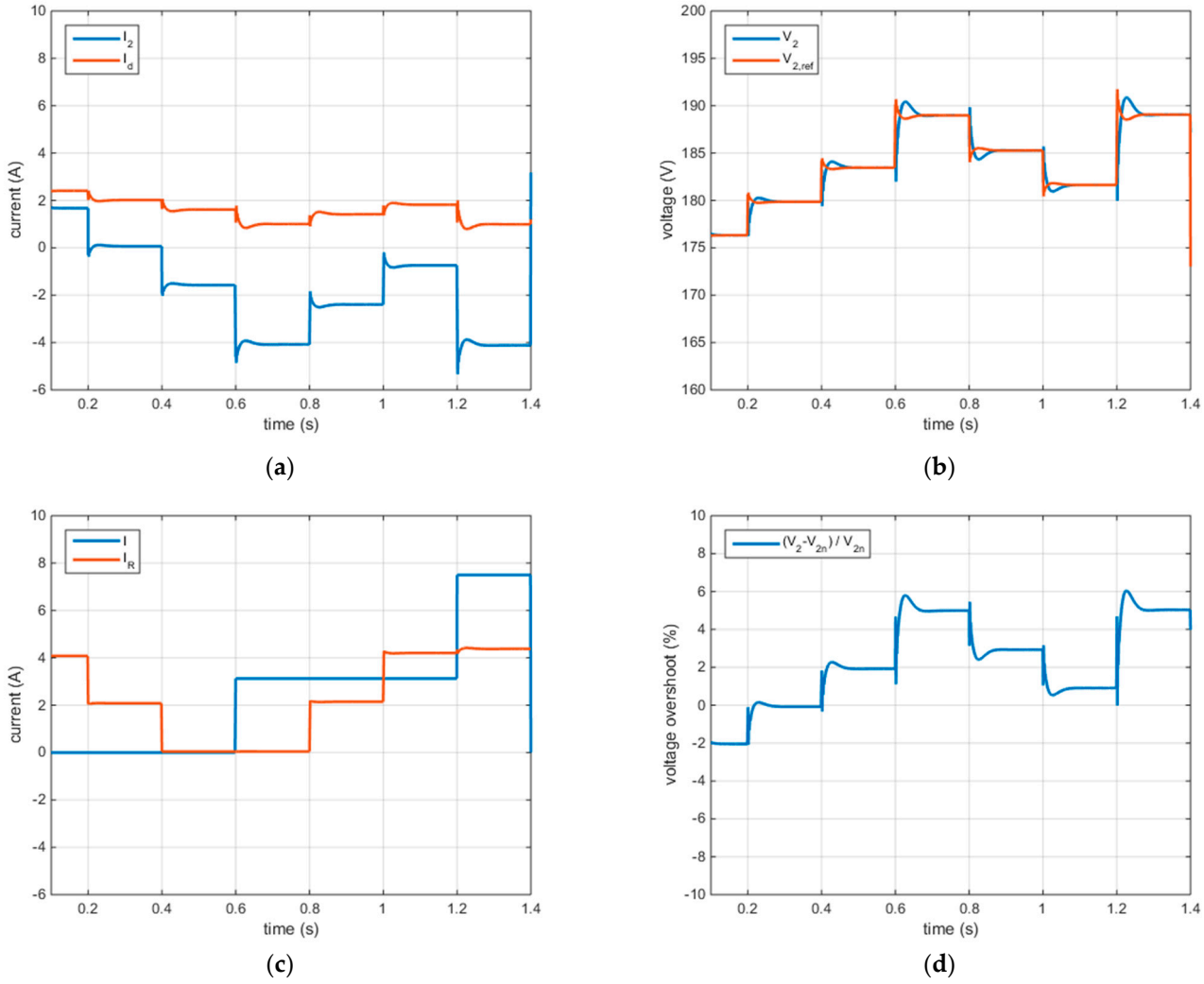

Figure 6. Performance obtained in scenario #3 (SD−GD): (**a**) output current and droop-controlled generator's current; (**b**) actual and reference grid voltage; (**c**) external generator's current and load current; (**d**) grid voltage overshoot.

4.4. Performance Assessment in Scenario #4 (SC-GD)

In scenario #4 (SC-GD), the voltage was regulated by the microgrid's equivalent voltage generator controlled in droop mode with non-null droop resistance. In contrast, the storage converter was operated as a current-controlled source based on a reference given by the EMS. Therefore, the control system of the Split-pi converter encompassed two loops for I_{L1} and I_{L2}, respectively. Furthermore, the presence of an equivalent external current generator in the microgrid was also considered.

The simulation results for this scenario are shown in Figure 7. Before t = 0.2 s, the converter output was at steady-state with the following values of load resistance, output current reference, and external current reference: $R = R_n$, $I_{2ref} = 0$, and $I = 0$. In other words, the storage system and the external current generator delivered no power while the load was supplied entirely by the equivalent voltage generator. Then, a representative sequence of R, I_{2ref}, and I values was applied, as shown in Table 5.

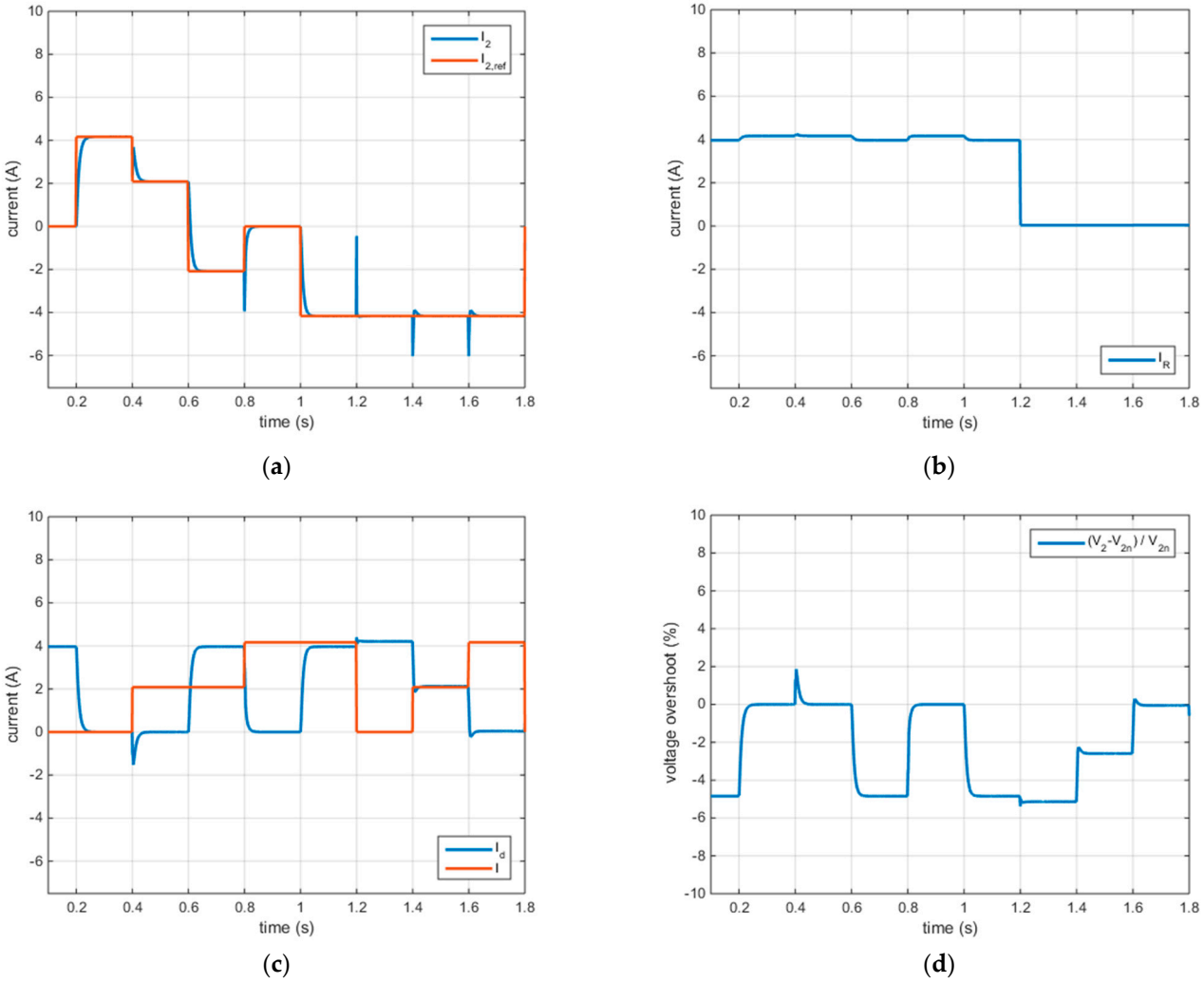

Figure 7. Performance obtained in scenario #4 (SC−GD): (**a**) actual and reference output current; (**b**) load current; (**c**) droop-controlled generator's current and external generator's current; (**d**) grid voltage overshoot.

Table 5. Transitions considered in scenario #4 (SC-GD).

Time (s)	Load Resistance	Expected Load Power	External Current Reference	Output Current Reference for the Converter
0.2	R_n	P_n	0	I_{2n}
0.4	R_n	P_n	$0.5 \cdot I_{2n}$	$0.5 \cdot I_{2n}$
0.6	R_n	P_n	$0.5 \cdot I_{2n}$	$-0.5 \cdot I_{2n}$
0.8	R_n	P_n	I_{2n}	0
1.0	R_n	P_n	I_{2n}	$-I_{2n}$
1.2	$100 \cdot R_n$	$P_n/100$	0	$-I_{2n}$
1.4	$100 \cdot R_n$	$P_n/100$	$0.5 \cdot I_{2n}$	$-I_{2n}$
1.6	$100 \cdot R_n$	$P_n/100$	I_{2n}	$-I_{2n}$

The load resistance kept the same value from t = 0.2 s to t = 1.2 s while the external current generator's reference progressively increased. Each time, the output current reference was set to the maximum value (either positive or negative) that respected the following conditions: it was compatible with the current combination of R and I, and it did not overload the droop-controlled generator and the storage system. From t = 1.2 s to t = 1.8 s, the load resistance was increased almost to a no-load condition, and the reference for the external current generator was progressively incremented. Again, the output current reference was set to the maximum value that did not overload the droop-controlled generator and the storage system; however, only negative values were allowed because of the no-load condition.

All the grid-side current transients were fast and clean even though challenging perturbations were applied, i.e., stepwise variations of circuit parameters. As for the microgrid voltage variation, Figure 7d shows that it went from −5.14% to 0% at steady-state with minimal over/undershoots, as expected. The FF action was not used with current-mode control; thus, the waveform of I_{L1} was like that obtained in the baseline scenario, and the waveform of the duty cycle was flat around its rated value.

4.5. Performance Assessment in Scenario #5 (SC-GS)

In this scenario, the storage converter was operated as a current-controlled source under the supervision of the EMS and connected to a microgrid in which one voltage generator was droop controlled with E_d = 180 V and R_d = 0 (stiff microgrid). Hence, model B was considered to design the control system. The initial condition was $I_{2ref} = 0$. Then, starting from t = 0.2 s, the same sequence of I_{2ref} as in scenario #4 (SC-GD) was applied, i.e., the one reported in the last column of Table 5. The simulation results for this scenario in terms of grid-side currents are shown in Figure 8 and confirmed the good system performance. The microgrid voltage V_2 was perfectly constant at 180 V because the voltage generator was controlled stiffly. Again, since the FF action was not used with current-mode control, the waveform of I_{L1} resembled that obtained in the baseline scenario. Furthermore, the duty cycle waveform was even flatter compared to the previous scenario because the converter had stiff voltages at both ports.

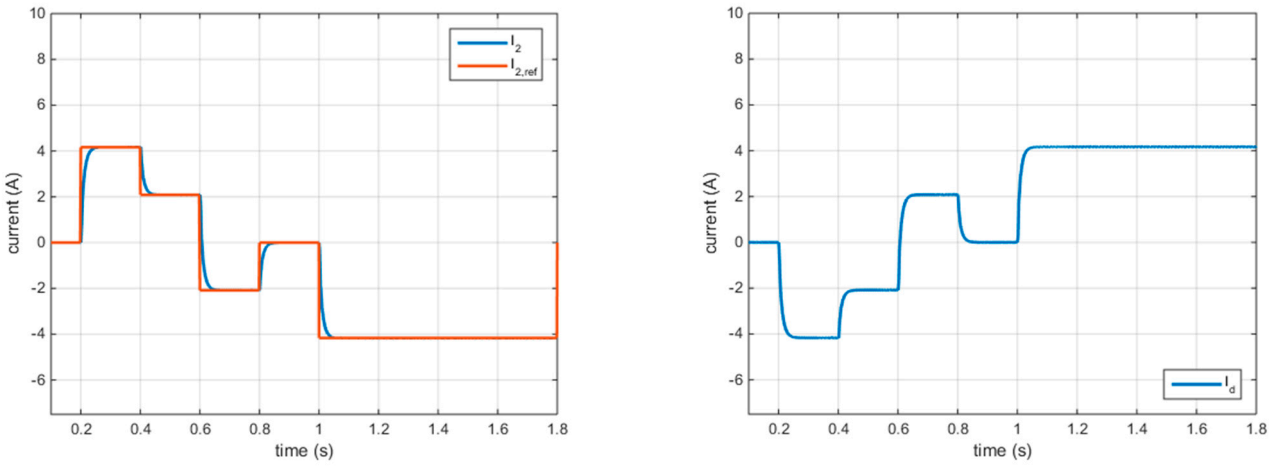

(**a**) (**b**)

Figure 8. Performance obtained in scenario #5 (SC−GS): (**a**) actual and reference output current; (**b**) droop-controlled generator's current.

4.6. Comparison among the Five Scenarios

The results obtained in the five scenarios were summarized in Table 6 for a comparison. The chosen metrics were the maximum charging/discharging power, the percentage voltage variation against V_{2n}, and the output voltage and current settling time. The latter metric is defined as the time after which the output variable enters and remains within a specified error band after applying an instantaneous stepwise input. The simulation results showed that some applied stimuli determined no difference between the steady-state value after the transition and the initial value. Therefore, the error band was defined summing/subtracting a fixed quantity to/from the steady-state value, as if it was a measurement error. Such a quantity was $0.01 \cdot V_{2n}$ for the output voltage and $0.01 \cdot I_{2n}$ for the output current.

Table 6. Result comparison in the five scenarios.

Scenario	Max. Charging or Discharging Power	Max. Voltage Variation due to Droop Control	Max. Instantaneous Voltage Variation Including over/Undershoot	Max. Settling Time of V_2	Max. Settling Time of I_2
#1 (SS-GN)	P_N	0%	+5%, −8.8%	16.6 ms	14 ms
#2 (SD-GN)	Slightly lower than P_N	±5%	±6.66%	56.2 ms	53 ms
#3 (SD-GD)	Charging up to P_N. Discharging at about half P_N	+5%, −2%	+6.05%, −3.05%	8 ms	57 ms
#4 (SC-GD)	P_N	0%, −5.14%	+1.867%, −5.383%	14.5 ms	41.9 ms
#5 (SC-GS)	P_N	0%	0%	Not applicable	47.6 ms

It is worth remarking that, in general, the microgrid designer cannot freely choose from all five scenarios due to system constraints. For example, the first three scenarios are impracticable if the designer decides to put the ESS converter under the control of an EMS; on the other hand, only the first and last scenarios are practicable if a stiff microgrid is to be designed. Thus, the proposed comparison can provide helpful information when the designer is not obliged to choose a specific scenario.

According to Table 6, the fastest performance was achieved in scenario #1 at the expense of the voltage variation, which can reach −8.8%. This behavior descended from the simplicity of such a scenario. Comparing scenarios #1 and #2 shows that introducing a virtual droop resistance dampened the system response and slightly reduced the maximum charging/discharging power as a side effect. Thus, the microgrid's voltage variation decreased, and the settling time increased for both V_2 and I_2 (+ 238% and +278%, respectively).

The use of more than one droop-controlled generator in the microgrid has pros and cons. In fact, in scenario #3, the maximum discharging power of the ESS was halved by design; thus, the ESS and its converter were partly underutilized. On the other hand, a halved maximum voltage reduction was exhibited, and the maximum settling time of V_2 decreased significantly (i.e., −52% and −86% compared to scenarios #1 and #2, respectively). The settling time reduction was achieved because the voltage waveform's peak did not surpass the tolerance band. Instead, the maximum settling time of I_2 stayed almost constant.

Comparing scenarios #2 and #3 with the last two scenarios showed a slight reduction of the settling time of I_2. Instead, a comparison between scenarios #4~#5 and scenario #1 revealed an increase of such a metric equal to +200% and +240%, respectively. As for the percentage voltage variation and the settling time of V_2 in scenario #4, they both exhibited intermediate values compared to scenarios #2 and #3. Finally, scenario #5 presented no voltage variation thanks to the stiff control of the microgrid.

Summing up, the following guidelines can be given for the considered case study. If the ESS converter must be controlled by an EMS, the response time of I_2 is around 50 ms, whereas that of V_2 does not exceed 15 ms and depends on the stiffness of the microgrid. Otherwise, the ESS converter should be operated in scenario #1 to achieve the fastest performance, i.e., around 15 ms response time for both V_2 and I_2. In such a scenario, the ESS converter is the only voltage source of the microgrid and is controlled stiffly. If these two conditions cannot be met, the response time of I_2 worsens significantly (around 60 ms), and the waveform of V_2 depends on a compromise: lower voltage variation and better dynamic performance come with a partial underutilization of the ESS.

5. Experimental Validation

The designed Split-pi converter is shown in Figure 9. It was built as a prototype using the components available in the lab, among them an integrated power module STGIPS10K60A encompassing an IGBT-based three-phase H-bridge. In order to validate

the converter and the related control laws experimentally, the storage system connected to port 1 was emulated using a TDK-Lambda GEN60-40 power supply (set to 50 V) and a parallel-connected 10 Ω, 300 W power resistor. The latter component was used to dissipate power during the recharge of the emulated storage system. On the other hand, a Sorensen SLH-500-6-1800 electronic load and a TDK-Lambda GEN600-5.5 power supply were connected to port 2 of the converter. The first device was used as the resistor R_{load} of the load model, whereas the other device was used as either the voltage generator E_d or the current generator I, depending on the specific test.

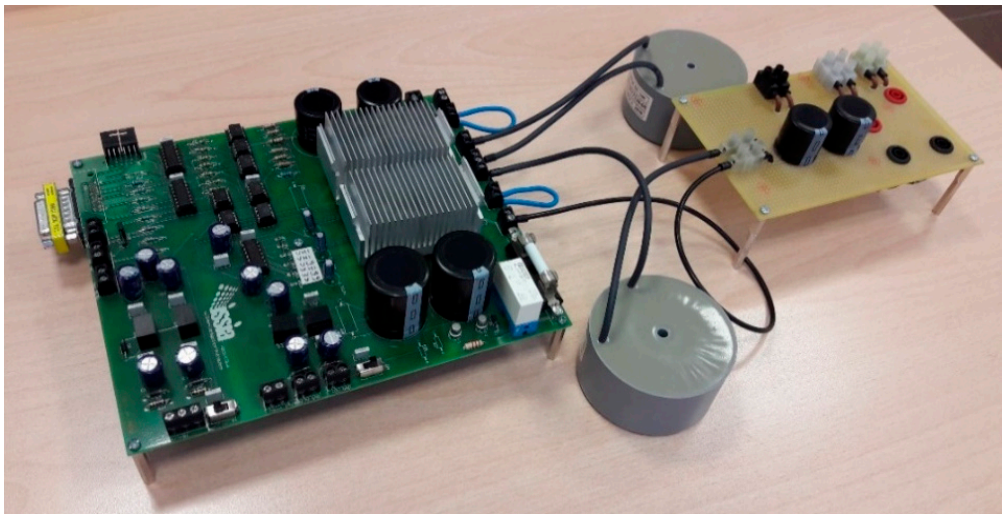

Figure 9. Picture of the realized Split-pi converter.

The control systems and the PWM modulator were implemented on a dSPACE DS1103 board connected to a desktop computer. Several electrical quantities were measured using LEM sensors, acquired and processed by the dSPACE board: I_{L1}, V_2, I_2, I_R. The current of the external generator was computed as $I_g = I_R - I_2$.

The prototypal Split-pi converter and the related control schemes were tested experimentally in several conditions covering the baseline and the other five scenarios. The obtained results showed good matching with the simulations presented in Section 4. Thus, they confirmed the good performance attainable in each scenario and, implicitly, the result comparison among the five scenarios. Furthermore, it is worth highlighting that a result comparison based on simulations rather than experiments inevitably gave a more accurate picture of the differences among the scenarios. In fact, the simulations allowed considering a much higher number of transients among operating conditions in each scenario compared to the experimental tests.

The waveforms of the most relevant signals acquired during the experimental tests were exported from dSPACE Control Desk to MATLAB and then plotted to analyze the results. The obtained plots are presented and commented on in the following.

5.1. Experimental Validation in the Baseline Scenario and Scenario #1 (SS-GN)

The Split-pi converter was used in these two tests to form a stiff microgrid supplying a passive load; no other generator was present in the microgrid. The converter was controlled using only the current and voltage loops in the baseline scenario, whereas the FF action was also included in scenario #1 (SS-GN). The electronic load was operated to reproduce a stepwise variation of load from 1300 Ω to 130 Ω; consequently, the load power instantly increased from 25 W to 250 W and produced a voltage undershoot.

The signals acquired during the tests are shown in Figure 10 and allow comparing the performance obtained with and without the FF action. All the waveforms were coherent with those obtained in the simulations. Thanks to the FF action, the reference for I_{L1} (and, in turn, the duty cycle) was instantly increased when the output current varied. Therefore,

in scenario #1 (SS-GN), the current waveforms were pretty squared, the voltage undershoot on V_2 was reduced from −5.73% to −1.86%, and the dynamics of V_2 were faster compared with the baseline scenario. An even higher under/overshoot reduction would be expected for higher stepwise variations of output power.

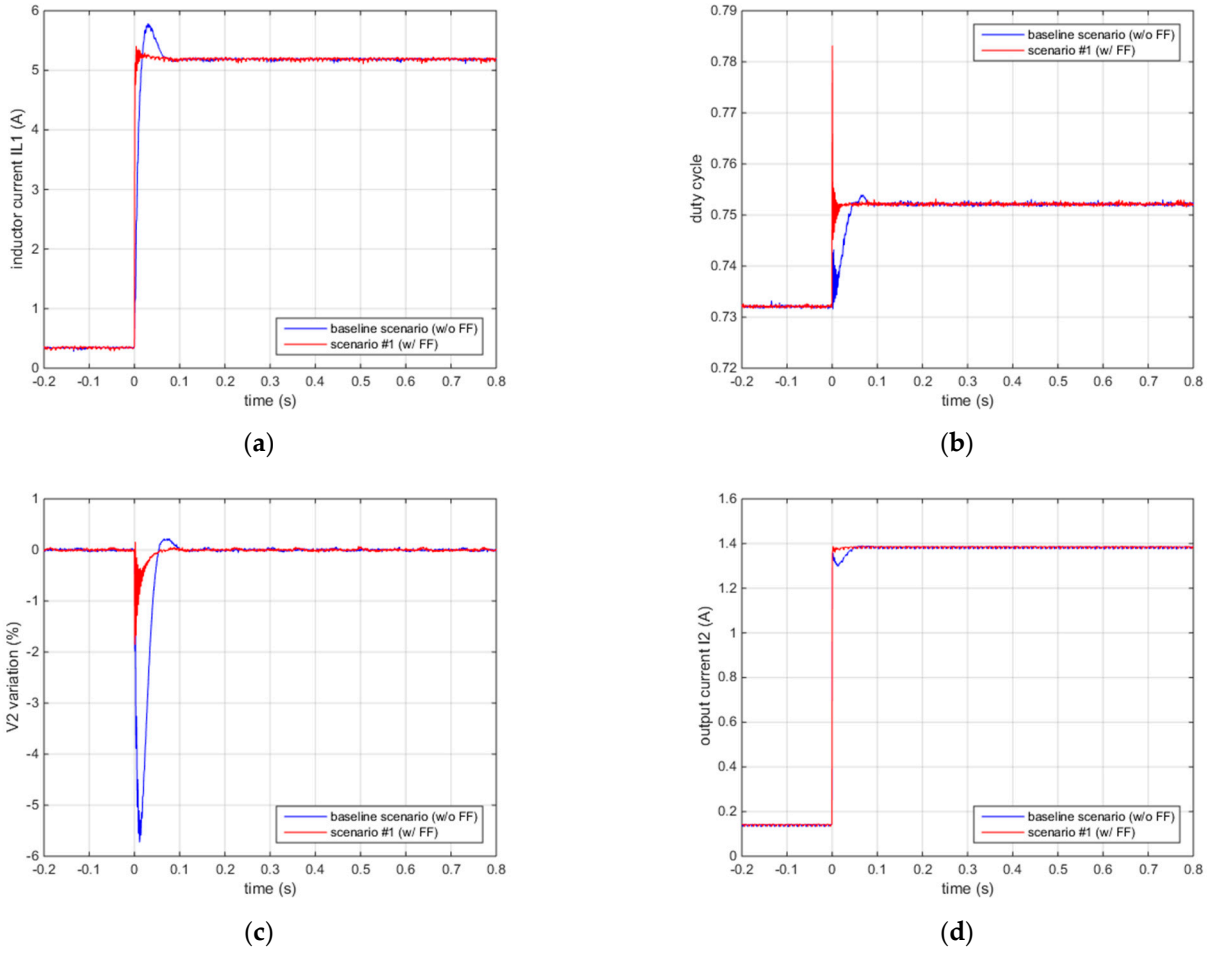

Figure 10. Experimental results in the baseline scenario and scenario #1 (SS−GN): (**a**) input inductor current; (**b**) duty cycle; (**c**) percentage variation of microgrid voltage; (**d**) grid−side current.

5.2. Experimental Validation in Scenario #2 (SD-GN)

In this test, the Split-pi converter was controlled using the FF action to form a non-stiff microgrid using a droop resistance of 1.33 Ω. The microgrid encompassed a passive load and an external power supply that was operated as a current generator. First, a current limit of 1.3 A and a voltage set point slightly higher than 180 V were set in the power supply; then, the device was turned on and off. The load resistance was 130 Ω, corresponding to a nominal current of about 1.385 A and a nominal power of 250 W.

The most relevant acquired signals are shown in Figure 11 and are coherent with those obtained in the simulations. Before t = 0 s, the load was entirely supplied by the converter. According to the droop resistance value, a 1.83 V voltage drop was exhibited, corresponding to a voltage variation of −1.02%; consequently, the load current was 1.375 A. At t = 0 s, the external current generator was turned on and supplied the load almost entirely, so the output current of the converter automatically dropped to almost zero. As a result, the voltage variation was almost zero, and the load current increased from 1.375 A to 1.382 A, reproducing the intended behavior. Finally, at about t = 1 s, the external current generator was turned off, and the converter took over the current again. In that condition, the load voltage and current again decreased slightly because of the droop control.

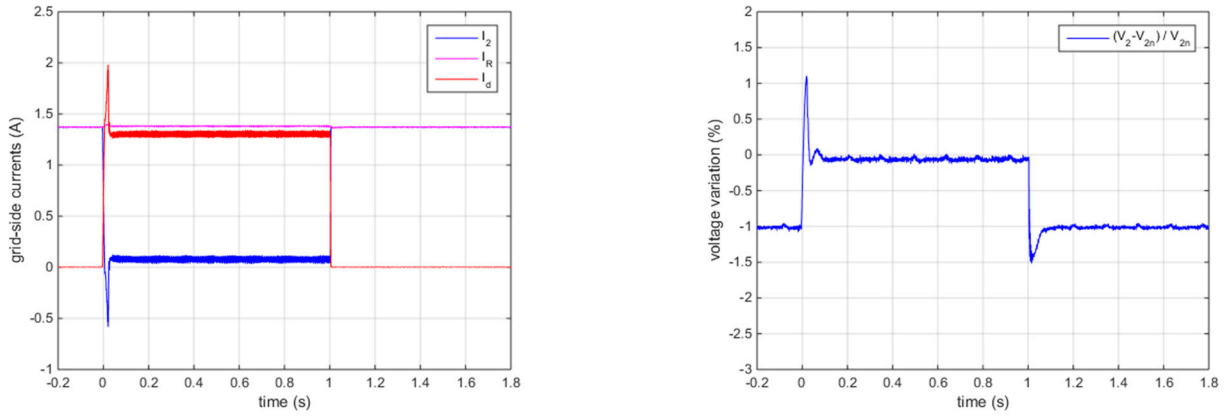

(**a**) (**b**)

Figure 11. Experimental results in scenario #2 (SD−GN): (**a**) grid−side currents; (**b**) percentage variation of microgrid voltage.

It is worth noting that the external power supply did not offer a proper current-mode operation; actually, it tried to impose the preset voltage (185 V) and continuously adjusted its output voltage aiming to respect the current limit. This behavior explains the initial peak in the generator's current. Nevertheless, the converter's control system was fast enough to effectively compensate for the connection and disconnection of the external generator. Therefore, the over/undershoot of microgrid voltage was minimal (+1.1% and −0.5%).

5.3. Experimental Validation in Scenario #3 (SD-GD)

In this test, the Split-pi converter and the microgrid voltage generator were controlled in droop mode with $R_d \neq 0$, so the resulting microgrid was not stiff. For the sake of clarity, a droop resistance of 1.33 Ω and a no-load voltage of 180 V were chosen as droop parameters for both devices. In this way, such devices always contributed equally to supplying the load. A stepwise variation of load resistance from 130 Ω to 260 Ω and back again was applied using the electronic load; this sequence corresponded to load power transitions from 250 W to 125 W and back again. The waveforms obtained in the test are shown in Figure 12 and show that the system exhibited good dynamic behavior, as expected based on the simulation results.

The system response was aperiodic, thanks to the high phase margin that was imposed. Furthermore, the current sharing ratio was respected for both load power values. Finally, the voltage variation at each power level was precisely the one expected according to the droop resistance value and the delivered current (−0.26% and −0.52%).

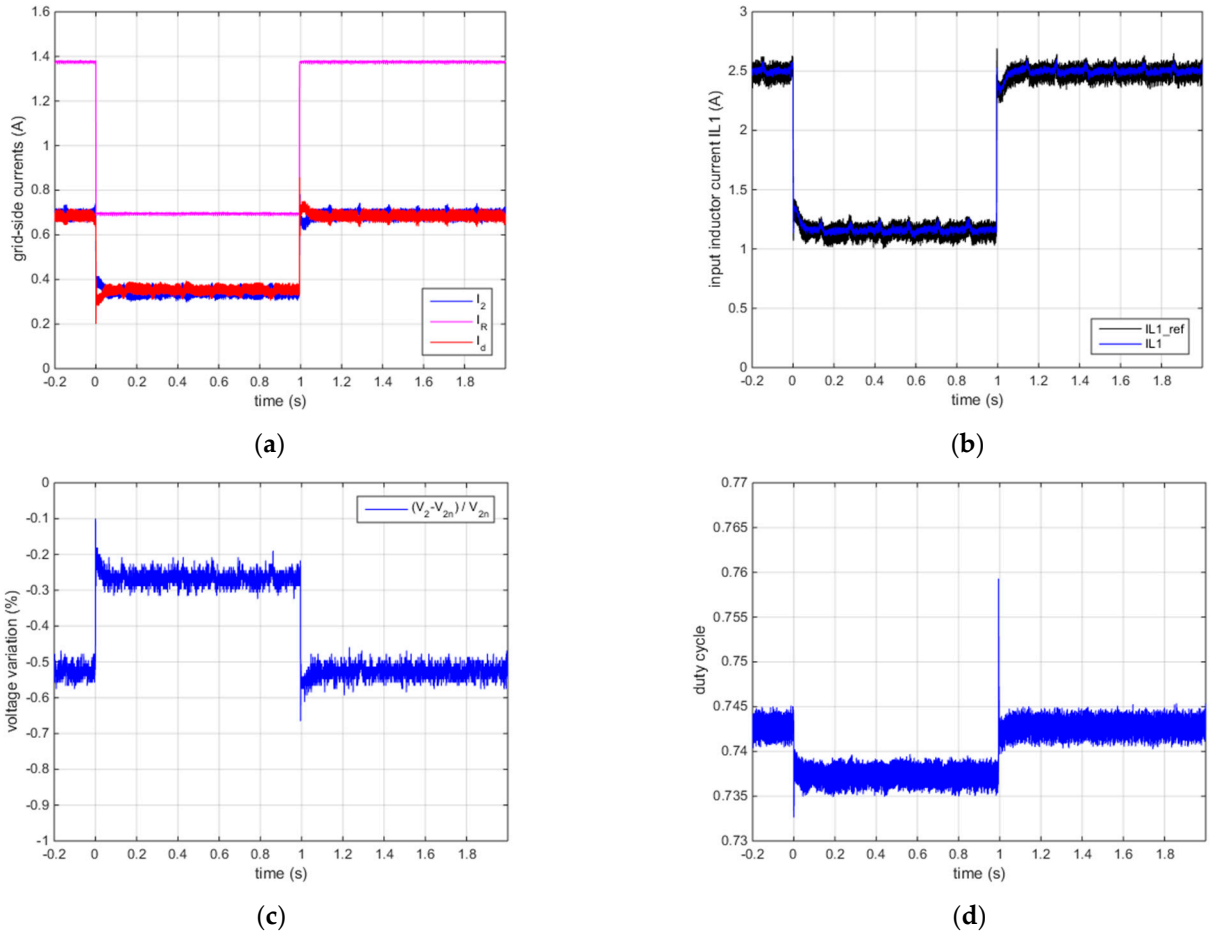

Figure 12. Experimental results in scenario #3 (SD−GD): (**a**) grid−side currents; (**b**) input inductor current; (**c**) percentage variation of microgrid voltage; (**d**) duty cycle.

5.4. Experimental Validation in Scenario #4 (SC-GD)

In this test, the Split-pi converter was operated as a current-controlled source exchanging power with a non-stiff microgrid. The external voltage generator was controlled in droop mode. The droop resistance was 1.33 Ω, and the no-load voltage was 180 V. The output current reference for the converter was changed at t = 0 s with a stepwise variation from −1.37 A to 1.37 A. Instead, the electronic load was operated to reproduce a stepwise variation of load resistance from 130 Ω to 65 Ω at about t = 0.7 s; these resistance values correspond to nominal load current (power) levels of 1.385 A (250 W) and 2.770 A (500 W), respectively.

The most relevant waveforms obtained in the test are presented in Figure 13 and are coherent with the simulation results. Before t = 0 s, the converter was controlled to draw −1.37 A from the DC microgrid recharging the emulated storage system. The external generator delivered 1.37 A to the converter and 1.345 A to the load for a total of 2.715 A. At t = 0 s, the current reference for the converter was increased to 1.37 A. Thus, the converter almost entirely supplied the load, and the current of the external generator automatically approached zero. Finally, at about t = 0.7 s, the load requested a current of 2.710 A. Since the converter's output was kept constant, the external generator automatically provided the additional current contribution of 1.34 A. In addition, the voltage variation was precisely the one expected according to the droop resistance value and the current supplied by the external voltage generator, i.e., −2%, 0%, and −1% for 2.715 A, 0 A, and 1.34 A, respectively. Furthermore, the system's dynamic behavior was good with fast aperiodic transients, coherently with the simulation results.

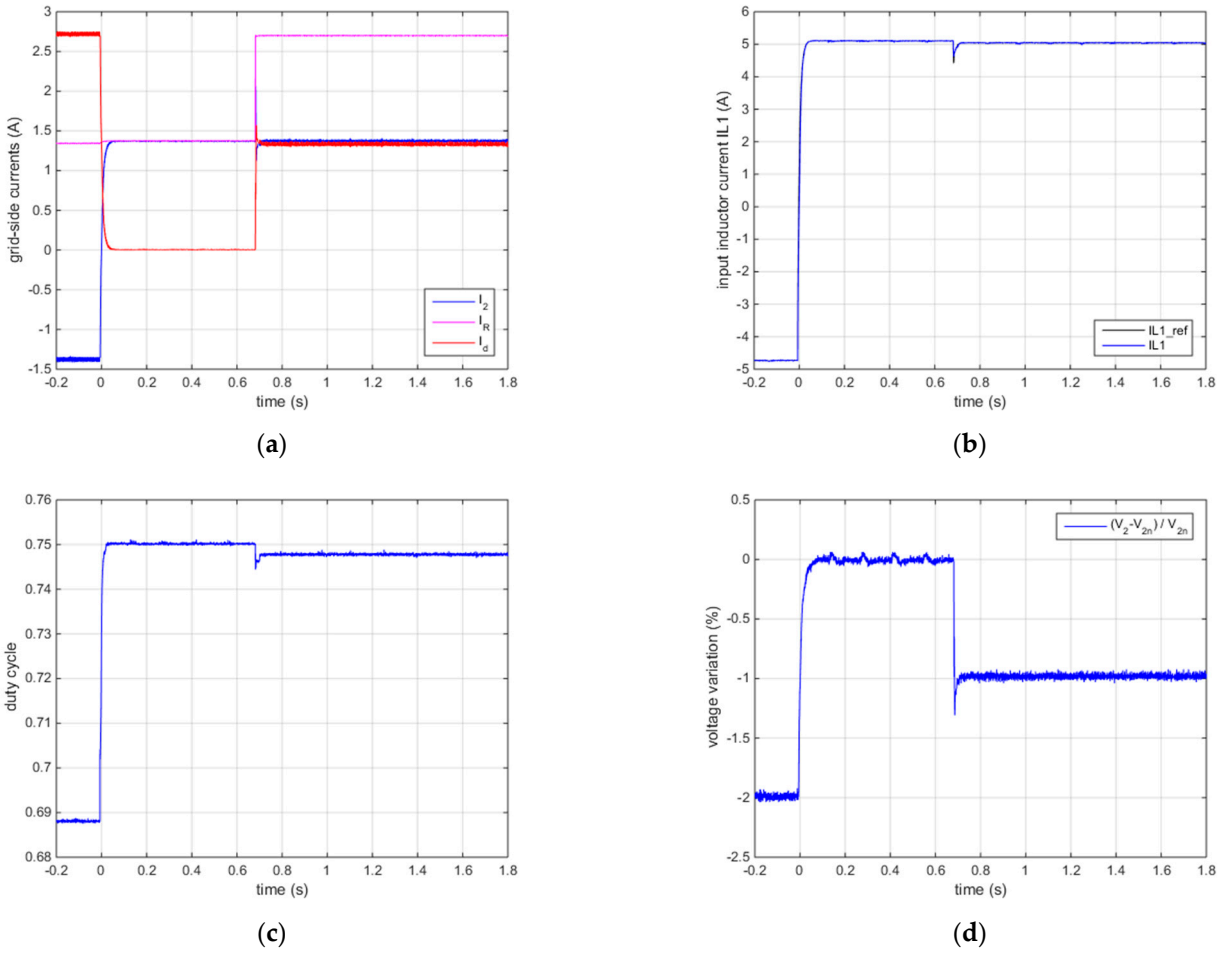

Figure 13. Experimental results in scenario #4 (SC−GD): (**a**) grid−side currents; (**b**) input inductor current; (**c**) duty cycle; (**d**) percentage variation of microgrid voltage.

5.5. Experimental Validation in Scenario #5 (SC-GS)

In this test, the Split-pi converter was operated as a current-controlled source exchanging power with a stiff microgrid. The external voltage generator still had a no-load voltage of 180 V but no droop resistance. The same combination of output current and load variations as in scenario #4 (SC-GD) was applied; however, the stepwise variation of load resistance occurred at about t = 1 s in scenario #5. Therefore, the output current reference was again changed with a stepwise variation from −1.37 A to 1.37 A at t = 0 s. Instead, the load resistance was varied from 130 Ω to 65 Ω at about t = 1 s, corresponding to nominal load current (power) levels of 1.385 A (250 W) and 2.770 A (500 W), respectively.

The most relevant among the acquired waveforms are presented in Figure 14. They are coherent with the simulation results and show that the converter's control system was also stable in this challenging condition. Furthermore, they are nearly identical to those of Figure 13; the main difference is the even smaller voltage variation, which determined slight differences in the load current and the external generator current. Before t = 0 s, the converter was controlled to draw −1.37 A from the DC microgrid recharging the emulated storage system. The external generator delivered 1.37 A to the converter and 1.385 A to the load for a total of 2.755 A. At t = 0 s, the current reference for the converter was increased to 1.37 A. Thus, the converter almost entirely supplied the load, and the current of the external generator automatically approached zero. Finally, at about t = 1 s, the load requested a current of 2.770 A. Since the converter's output was kept constant, the external generator automatically provided the additional current contribution of 1.385 A.

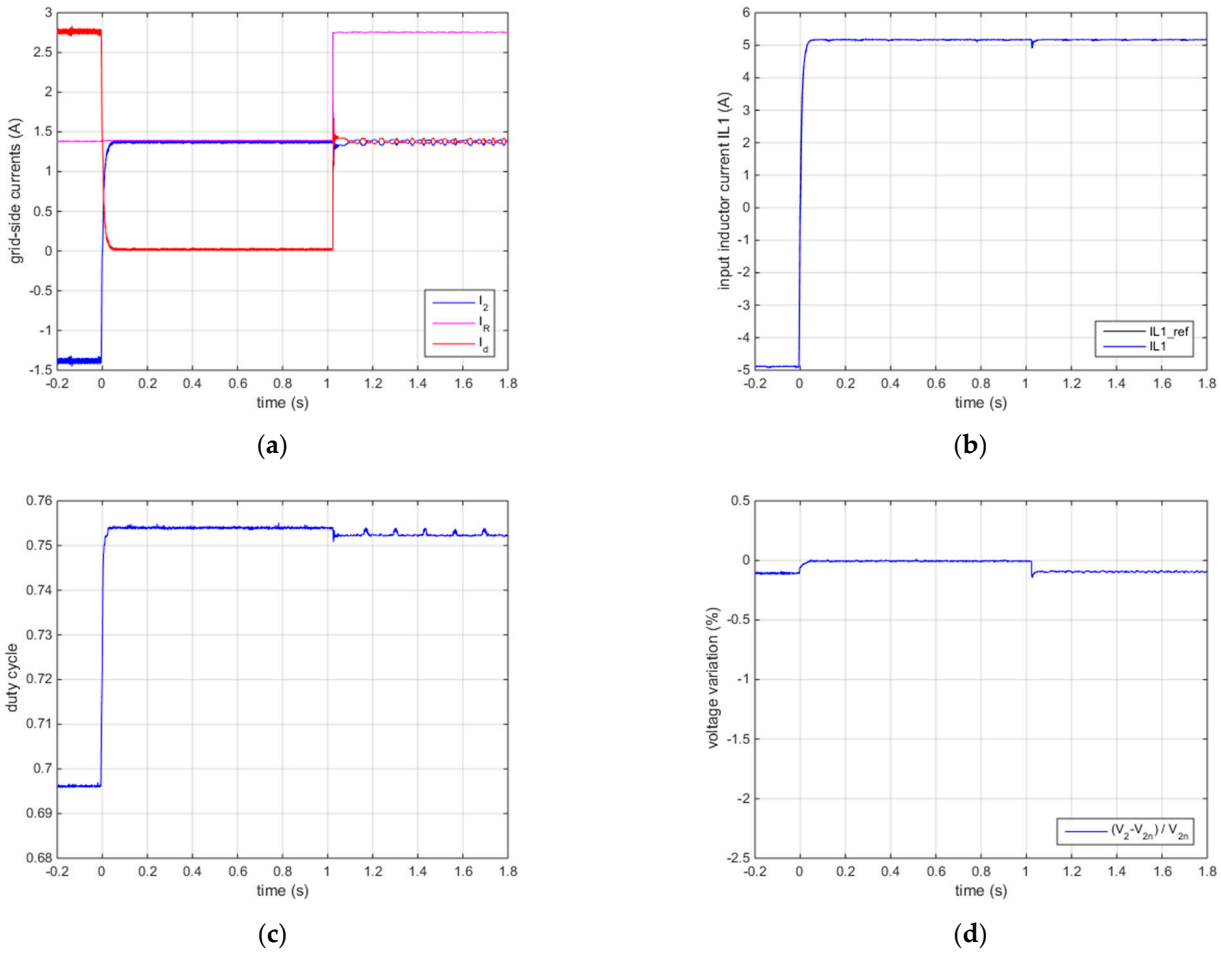

Figure 14. Experimental results in scenario #5 (SC−GS): (**a**) grid−side currents; (**b**) input inductor current; (**c**) duty cycle; (**d**) percentage variation of microgrid voltage.

In this scenario, the theoretical voltage variation was 0% because the DC microgrid was stiff. However, a small resistance was present due to cable connections. Nonetheless, the actual voltage variation was −0.1%, as shown in Figure 14d. Again, the system exhibited good dynamic behavior with fast aperiodic transients, as expected based on the simulation results.

6. Conclusions

The Split-pi converter is a good choice to integrate an energy storage system (ESS) into a DC microgrid. In part I of this work, five typical microgrid scenarios were identified. Each of them required a specific state-space model of the Split-pi and a suitable control scheme. Two different state-space models were devised for the Split-pi converter operating with lower storage-side voltage than grid-side voltage. Such models considered the parasitic elements of the converter. In addition, the most relevant transfer functions were given, together with control schemes with a different number of control loops and criteria to design the controllers.

The present paper completed the study validating the theoretical analysis based on comprehensive simulations and experimental tests. A 48 V, 750 W storage system interfaced with a 180 V DC microgrid using a Split-pi converter was chosen as a case study. It can represent a reduced-power prototype of terrestrial and marine microgrids. Several simulations were performed to assess the system performance in all the considered scenarios. Furthermore, a prototypal Split-pi converter was realized, and experimental tests were performed in conditions that covered all the scenarios. The obtained results were coherent with the simulations and validated the study.

Further activities will include theoretical studies and experiments with a twofold aim: (1) to devise the state-space model of the Split-pi operating with higher storage-side voltage than grid-side voltage; (2) to investigate the possibility of designing unconventional control systems for the Split-pi that are suitable for operating in more than one microgrid scenario.

Author Contributions: Conceptualization, M.L., A.S., M.P. and M.C.D.P.; methodology, M.L., A.S. and A.A.; software, M.L., A.S., A.A. and G.L.T.; validation, M.L., A.A., M.C.D.P. and M.P.; Writing—Original draft preparation, M.L., A.S. and M.P.; Writing—Review and Editing, M.L., A.A., M.C.D.P. and G.L.T.; supervision, M.P. and M.L.; funding acquisition, M.P. and M.L. All authors have read and agreed to the published version of the manuscript.

Funding: This research was funded by the Italian Ministry of University and Research (MUR), program PON R&I 2014/2020-Avviso n. 1735 del 13/07/2017-PNR 2015/2020, project "NAUSICA-NAvi efficienti tramite l'Utilizzo di Soluzioni tecnologiche Innovative e low CArbon," CUP: B45F21000680005.

Institutional Review Board Statement: Not applicable.

Informed Consent Statement: Not applicable.

Data Availability Statement: Not applicable.

Conflicts of Interest: The authors declare no conflict of interest.

References

1. Anand, S.; Fernandes, B.G. Optimal voltage level for DC microgrids. In Proceedings of the IECON 2010—36th Annual Conference on IEEE Industrial Electronics Society, Glendale, AZ, USA, 7–10 November 2010; pp. 3034–3039.
2. Sharma, A.; Singh, S.N.; Srivastava, S.C. Optimal Selection of DC Microgrid Architecture. In Proceedings of the 8th IEEE Power India International Conference (PIICON 2018), Kurukshetra, India, 10–12 December 2018; pp. 1–5.
3. Wang, H.; Zhang, T.; Zhang, B. Selection of DC Voltage Level in household Hybird AC/DC power supply system. In Proceedings of the 2019 IEEE 8th International Conference on Advanced Power System Automation and Protection (APAP), Xi'an China, 21–24 October 2019; pp. 1527–1530.
4. D.O.D. of United States of America. Military Std. MIL-STD-704F. In *Dep. Def. Interface Stand. Aircraft Electr. Power Charact*; D.O.D. of United States of America: Arlington County, VA, USA, 2004.
5. Ballou, P.J. A specialized ROV for inspection of salt dome caverns. In Proceedings of the IEEE Oceanic Engineering Society. OCEANS'98. Conference Proceedings (Cat. No.98CH36259), Nice, France, 28 September–1 October 1998; pp. 1584–1588.
6. Lin, M.; Lin, R.; Chen, L.; Yang, C.; Li, D. Underwater Docking System with Bidirectional Wireless Power Transmission Capability. In Proceedings of the Global Oceans 2020: Singapore—U.S. Gulf Coast, Biloxi, MS, USA, 5–30 October 2020; pp. 1–5.
7. Zadeh, M.K.; Zahedi, B.; Molinas, M.; Norum, L.E. Centralized stabilizer for marine DC microgrid. In Proceedings of the IECON 2013—39th Annual Conference of the IEEE Industrial Electronics Society, Vienna, Austria, 10–13 November 2013; pp. 3359–3363.
8. Wang, L. Dynamic analysis of a Microgrid system for supplying electrical loads in a sailing boat. In Proceedings of the IEEE Power Energy Society General Meeting, San Diego, CA, USA, 22–26 July 2012; pp. 1–7.
9. Xue, L.; Baxter, B.; Torrano, K.; Yao, G. A power management strategy of an onboard DC microgrid. In Proceedings of the IECON 2017—43rd Annual Conference of the IEEE Industrial Electronics Society, Beijing, China, 29 October–1 November 2017; pp. 6759–6764.
10. Kim, S.; Kucka, J.; Ulissi, G.; Kim, S.-N.; Dujic, D. Solid-State Technologies for Flexible and Efficient Marine DC Microgrids. *IEEE Trans. Smart Grid* **2021**, *12*, 2860–2868. [CrossRef]
11. Zeng, Y.; Zhang, Q.; Liu, Y.; Zhuang, X.; Lv, X.; Wang, H. Distributed Secondary Control Strategy for Battery Storage System in DC Microgrid. In Proceedings of the 2021 IEEE 4th International Electrical and Energy Conference (CIEEC), Wuhan, China, 28–30 May 2021; pp. 1–7.
12. D'Agostino, F.; Schiapparelli, G.P.; Silvestro, F.; Grillo, S. DC Shipboard Microgrid Modeling for Fuel Cell Integration Study. In Proceedings of the 2019 IEEE Power & Energy Society General Meeting (PESGM), Atlanta, GA, USA, 4–8 August 2019; pp. 1–5.
13. Di Piazza, M.C.; Luna, M.; Pucci, M.; La Tona, G.; Accetta, A. Electrical Storage Integration into a DC Nanogrid Testbed for Smart Home Applications. In Proceedings of the 2018 IEEE International Conference on Environment and Electrical Engineering and 2018 IEEE Industrial and Commercial Power Systems Europe (EEEIC / I&CPS Europe), Palermo, Italy, 12–15 June 2018; pp. 1–5.
14. Chub, A.; Vinnikov, D.; Kosenko, R.; Liivik, E.; Galkin, I. Bidirectional DC–DC Converter for Modular Residential Battery Energy Storage Systems. *IEEE Trans. Ind. Electron.* **2020**, *67*, 1944–1955. [CrossRef]
15. Sim, J.; Lee, J.; Choi, H.; Jung, J.H. High Power Density Bidirectional Three-Port DC-DC Converter for Battery Applications in DC Microgrids. In Proceedings of the 2019 10th International Conference on Power Electronics and ECCE Asia (ICPE 2019 - ECCE Asia), Busan, Korea, 27–30 May 2019; pp. 843–848.
16. Byrne, R.H.; Nguyen, T.A.; Copp, D.A.; Chalamala, B.R.; Gyuk, I. Energy Management and Optimization Methods for Grid Energy Storage Systems. *IEEE Access* **2018**, *6*, 13231–13260. [CrossRef]

17. La Tona, G.; Luna, M.; Di Piazza, A.; Di Piazza, M.C. Towards the real-world deployment of a smart home EMS: A DP implementation on the Raspberry Pi. *Appl. Sci.* **2019**, *9*, 2120. [CrossRef]
18. Accetta, A.; Pucci, M. Energy Management System in DC Micro-Grids of Smart Ships: Main Gen-Set Fuel Consumption Minimization and Fault Compensation. *IEEE Trans. Ind. Appl.* **2019**, *55*, 3097–3113. [CrossRef]
19. Crocker, T.R. Power Converter and Method for Power Conversion. U.S. Patent No. 20040212357A1, 28 October 2004.
20. Khan, S.A.; Pilli, N.K.; Singh, S.K. Hybrid Split Pi converter. In Proceedings of the 2016 IEEE International Conference on Power Electronics, Drives and Energy Systems (PEDES), Trivandrum, India, 14–17 December 2016; pp. 1–6.
21. Sobhan, S.; Bashar, K.L. A novel Split-Pi converter with high step-up ratio. In Proceedings of the 2017 IEEE Region 10 Humanitarian Technology Conference (R10-HTC), Dhaka, Bangladesh, 21–23 December 2017; pp. 255–258.
22. Ahmad, T.; Sobhan, S. Performance analysis of bidirectional split-Pi converter integrated with passive ripple cancelling circuit. In Proceedings of the 2017 International Conference on Electrical, Computer and Communication Engineering (ECCE), Cox's Bazar, Bangladesh, 16–18 February 2017; pp. 433–437.
23. Singhai, M.; Pilli, N.; Singh, S.K. Modeling and analysis of split-Pi converter using State space averaging technique. In Proceedings of the 2014 IEEE International Conference on Power Electronics, Drives and Energy Systems (PEDES), Mumbai, India, 16–19 December 2014; pp. 1–6.
24. Maclaurin, A.; Okou, R.; Barendse, P.; Khan, M.A.; Pillay, P. Control of a flywheel energy storage system for rural applications using a Split-Pi DC-DC converter. In Proceedings of the 2011 IEEE International Electric Machines & Drives Conference (IEMDC), Niagara Falls, ON, Canada, 15–18 May 2011; pp. 265–270.
25. Sabatta, D.; Meyer, J. Super capacitor management using a Split-Pi symmetrical bi-directional DC-DC power converter with feed-forward gain control. In Proceedings of the 2018 International Conference on the Domestic Use of Energy (DUE), Cape Town, South Africa, 3–5 April 2018; pp. 1–5.
26. Monteiro, V.; Oliveira, C.; Rodrigues, A.; Sousa, T.J.C.; Pedrosa, D.; Machado, L.; Afonso, J.L. A Novel Topology of Multilevel Bidirectional and Symmetrical Split-Pi Converter. In Proceedings of the 2020 IEEE 14th International Conference on Compatibility, Power Electronics and Power Engineering (CPE-POWERENG), Setubal, Portugal, 8–10 July 2020; pp. 511–516.
27. Alzahrani, A.; Shamsi, P.; Ferdowsi, M. Single and interleaved split-pi DC-DC converter. In Proceedings of the 2017 IEEE 6th International Conference on Renewable Energy Research and Applications (ICRERA), San Diego, CA, USA, 5–8 November 2017; pp. 995–1000.
28. Luna, M.; Sferlazza, A.; Accetta, A.; Di Piazza, M.C.; La Tona, G.; Pucci, M. Modeling and Performance Assessment of the Split-Pi Used as a Storage Converter in All the Possible DC Microgrid Scenarios. Part I: Theoretical Analysis. *Energies* **2021**, *14*, 4902. [CrossRef]
29. Khooban, M.H.; Gheisarnejad, M.; Farsizadeh, H.; Masoudian, A.; Boudjadar, J. A New Intelligent Hybrid Control Approach for DC–DC Converters in Zero-Emission Ferry Ships. *IEEE Trans. Power Electron.* **2020**, *35*, 5832–5841. [CrossRef]